



Construction of dual defect mediated Z-scheme photocatalysts for enhanced photocatalytic hydrogen evolution

Huihui Gao^{a,1}, Ruya Cao^{a,c,1}, Xuetao Xu^b, Shouwei Zhang^{a,*}, Yongshun Huang^c, Hongcen Yang^{a,c}, Xiaolong Deng^a, Jiaxing Li^{c,d,*}

^a School of Physics and Technology, University of Jinan, Shandong, 250022, PR China

^b School of Chemical and Environmental Engineering, Wuyi University, Jiangmen, 529020, PR China

^c CAS Key Laboratory of Photovoltaic and Energy Conservation Materials, Institute of Plasma Physics, Chinese Academy of Sciences, P.O. Box 1126, 230031, Hefei, PR China

^d Collaborative Innovation Center of Radiation Medicine of Jiangsu Higher Education Institutions, School for Radiological and Interdisciplinary Sciences, Soochow University, Suzhou, 215123, PR China



ARTICLE INFO

Keywords:

Dual defect
Direct Z-scheme
Oxides/g-C₃N₄
Heterojunction
Photocatalytic hydrogen evolution

ABSTRACT

The construction of Z-scheme system is a promising approach for photocatalytic hydrogen evolution (PHE). In this study, we fabricated a direct Z-scheme system consisting of defect-rich g-C₃N₄ nanosheets (DR-CNNS) crumpled nanosheets with defect-rich TiO₂ (DR-TiO₂) nanoparticles via a dual defective strategy. The optimized dual-defective rich TiO₂/CNNS composite showed a superior PHE rate of ~651.79 μmol/h with a turnover frequency of ~419.3 h⁻¹ as well as high stability and recyclability, which presented the highest value in single defective TiO₂ or g-C₃N₄-based photocatalysts families reported previously. Furthermore, this protocol could also be extended to synthesize other dual defective g-C₃N₄/oxides (ZnO, SnO₂, etc.) heterostructures. The improved photocatalytic performances could be ascribed to the following aspects: (1) rich dual defect, narrowing the band gap and providing more reactive sites for PHE; (2) intimate interface, facilitating interfacial migration and utilization of photogenerated charges; (3) Z-scheme structure, accelerating photogenerated electron-hole pair separation and thus leading to more efficient PHE. Our work highlights the critical role of defects in construction of Z-scheme system and provides the possibility of utilizing dual defective g-C₃N₄-based systems for other photocatalytic applications including CO₂ reduction and water purification.

1. Introduction

Energy and environmental crises resulting from the consumption of traditional fossil fuels cause an adverse effect on the environment and urge us to seek renewable and environmentally friendly energy resources [1–3]. Photocatalytic hydrogen evolution (PHE) has boosted explosive interests as a clean energy production approach [4–6]. Unfortunately, the low H₂ evolution and low utilization efficiency of sunlight greatly limited the potential practical applications. Therefore, the development of novel photocatalysts with high photocatalytic activity and/or wide spectrum response became a crucial issue.

Defect engineering can modulate the performance of photocatalytic materials by extending the spectral response and improving the photogenerated charges separation and transfer efficiency as well as producing more surface reactions [4,7–12]. For example, the spectral

response of oxides could be greatly expanded by implanting defects [7,13–17]. Moreover, defects have also been reported to boost catalytic activity by taking advantage of defect sites as active centers [4,7,18]. For example, oxygen vacancies in oxide photocatalysts have been reported to play an important part in improving photocatalytic performance [19–21]. In 2011, Chen et al. found that the hydrogenated black TiO₂ nanoparticles have higher photocatalytic performances in degrading pollutants and photocatalytic H₂ evolution [22]. Since then, great effort had been made to design and synthesize black TiO₂-based materials for photocatalytic water splitting [5,21]. For instance, Huang's group had successfully synthesized various morphological black TiO₂ photocatalysts, including nanoparticles, platelike, nanowire, and hexagonal nanosheets, which showed excellent degradation properties [5,23]. Ordered mesoporous hydrogenated black TiO₂ was prepared by Zhou et al., which exhibited a high H₂ evolution rate

* Corresponding authors.

E-mail addresses: sps_zhangsw@ujn.edu.cn (S. Zhang), lijx@ipp.ac.cn (J. Li).

¹ These authors contributed equally to this work.

(136.2 $\mu\text{mol}/\text{h}$) [24]. Important progress had been made in the preparation of defective TiO_2 for enhanced photocatalysis; however, its photocatalytic performance was still inevitably limited by photo-generated charge separation efficiency, which was a major disadvantage of TiO_2 as a single-component photocatalyst [25]. Coupling defective TiO_2 with other appropriate semiconductors to form heterostructure may be an effective strategy for enhancing photogenerated charge separation and migration efficiency [26].

Graphitic carbon nitride ($\text{g-C}_3\text{N}_4$) with 2D layered structures has particularly attractive and widely used in PHE due to its suitable band gap and band edge positions as well as excellent thermal and chemical stability [2,27–30]. However, the high recombination rates of photo-generated charges and limited light response confined its photocatalytic activity and practical applications [27,31]. Accordingly, various solutions, such as doping metal/non-metal elements, constructing heterostructures or optimizing morphologies etc., have been reported to enhance its photocatalytic performance [2,28,32–36]. Recently, several literatures indicated that the introduction of defects in $\text{g-C}_3\text{N}_4$ could notably boost its photocatalytic performance [8,27,37–40]. For instance, carbon vacancies can significantly enhanced PHE activity of $\text{g-C}_3\text{N}_4$ [41]. Nitrogen-deficient $\text{g-C}_3\text{N}_x$ was prepared through the alkaline-assisted polymerization method, which exhibited obviously red-shifted absorption edge [42]. Furthermore, the defects could also act as specific reactive sites for reactant molecules in the photocatalytic process [4,8,43]. Therefore, considering the characteristics of defective TiO_2 and $\text{g-C}_3\text{N}_4$, coupling defective TiO_2 with defective $\text{g-C}_3\text{N}_4$ to form dual defective heterostructure is highly anticipated to optimize the photocatalytic activity, but has rarely been reported.

As we known, Z-scheme heterojunction system have many advantages, such as enhanced light response, spatially separated active sites and stronger redox ability etc., all of which contribute to photocatalytic activity [40–51]. However, the construction of non-intimate contact interfaces in composites remains one of the biggest challenges in the development of efficient Z-scheme photocatalytic system [52]. Fortunately, a large number of defects in composite can not only facilitate the formation of intimate contact, but also can effectively adjust the semiconductor energy level to form the defect-mediated Z-scheme systems. However, although improved PHE activity by single defective Z-scheme systems was realized, introducing dual defect in composites to construct innovative Z-scheme systems has rarely been reported.

Directed by the above strategy, it was proposed in this work to anchor defect-rich TiO_2 (DR- TiO_2) on ultrathin defect-rich $\text{g-C}_3\text{N}_4$ nanosheets (DR-CNNS), which was expected to exhibit synergistic effect on boosting water splitting. This dual defective construction achieved intimate interface between the two components, thus photogenerated electrons could easily separate and transfer through the interface to abundant active defect sites and induced H_2 evolution. The dual defective system exhibit efficient solar light harvesting, as well as impressively enhanced PHE activity and stability. The photogenerated charges transfer and separation efficiency was also investigated by various optical and electrochemical analyses, and the Z-scheme mechanism was also investigated.

2. Experimental section

2.1. Synthesis of dual defect rich TiO_2 /CNNS composites

The CNNS were prepared from urea via thermal method, as reported previously [25]. To prepare the dual defective rich TiO_2 /CNNS composites, CNNS (700 mg), TiO_2 (300 mg) and NaBH_4 (500 mg) were ground in a mortar to form a uniform distribution and placed into a quartz boat inside the tube furnace. Subsequently, the samples were maintained at 300 °C for 50 min under Ar atmosphere. The samples were washed with water to remove impurities. In all runs, the total amounts of CNNS + TiO_2 were kept constant of 1 g by changing the mass ratio of CNNS/ TiO_2 (from 9:1 to 5:5), while the amounts of NaBH_4

was held constant. The prepared dual-defective rich TiO_2 /CNNS composites were denoted as DDR-xCyT (x:y = 9:1, 8:2, 7:3, 6:4 and 5:5).

Single defective systems, including defective TiO_2 /CNNS (DR- TiO_2 /CNNS) or TiO_2 /defective CNNS (TiO_2 /DR-CNNS), were obtained. The synthetic process was as follows. DR-CNNS (700 mg) and TiO_2 (300 mg) or CNNS (700 mg) and DR- TiO_2 (300 mg) were ground in an agate mortar for 60 min. Finally, the TiO_2 /DR-CNNS were obtained by annealing mixture at 300 °C in Ar for 50 min. DR- TiO_2 /CNNS was obtained via the same procedure, except that DR- TiO_2 and CNNS were used as the precursors. Controlled DR-CNNS or DR- TiO_2 photocatalysts were obtained via the same procedure in the absence of TiO_2 or CNNS, respectively.

The mechanical mixture of DR-CNNS (700 mg) and DR- TiO_2 (300 mg) (defined as DR-CNNS + DR- TiO_2) was prepared by physical grind in agate mortar for 60 min.

2.2. Characterization

X-ray diffraction (XRD) patterns were performed on X-ray diffractometer (Miniflex 600, Rigaku) using $\text{Cu-K}\alpha$ radiation ($\lambda = 1.54178 \text{ \AA}$). The functional groups was measured by Fourier transform infrared spectroscopy (FTIR, Thermo Nicolet). The transmission electron microscopy (TEM) was measured by using a JEOL-TEM 2010 F. The scanning electron microscopy (SEM) images were obtained by JSM-7500. Chemical characterization of the sample surface was performed using an X-ray photoelectron spectroscopy (XPS Thermo Fisher ESCALAB 250Xi). UV-vis diffuse reflection spectra (DRS) were recorded on a Shimadzu UV-2550 UV-vis spectrophotometer. The electronic spin resonance (ESR) measurements were carried out at room temperature on a JEOL JES-FA-200. The photoluminescence (PL) spectra and time-resolved PL (TRPL) spectra were obtained using an Edinburgh FLS980 spectrophotometer. The electrochemical measurements were performed on a CHI660E electrochemical system using three-electrode system. For all of the measurements, the electrolyte was a 0.5 M Na_2SO_4 solution. The sample for ESR measurement was prepared by mixing photocatalysts in a 50 mM 5, 5-dimethyl-1-pyrroline N-oxide (DMPO) solution with aqueous dispersion for DMPO-OH^\cdot and methanol dispersion for DMPO-O_2^\cdot .

2.3. Photocatalytic activity evaluation

Typically, the photocatalysts (10 mg) were added in triethanolamine (TEOA) aqueous solution (10 vol. %). Co-catalysts Pt (~3 wt. %) was loaded on the surface of catalyst via an *in situ* photo-deposition method with H_2PtCl_6 . The residual air in the reactor was removed by vacuuming the system before the reaction was triggered under irradiation. A 300 W Xe lamp (PLS-SXE, Perfectlight, China) was served as light source. The average irradiation intensity was ~27.34 mW/cm² (irradiation area was ~15.9 cm²). The amount of evolved H_2 was quantitatively analyzed in an interval time of 30 min by an online gas chromatography (GC-7900) with high-purity nitrogen carrier gas.

3. Results and discussion

XRD patterns of as-prepared photocatalysts were shown in Fig. 1A–C. The strong peaks indicated that pristine TiO_2 was highly crystalline as P25 TiO_2 (Fig. 1A). New peaks observed in DR- TiO_2 could be attributed to reduced titanium oxides, such as Ti_9O_{17} , Ti_8O_{15} , and Ti_3O_5 (Fig. 1A) [13]. For pure CNNS (Fig. 1B), the typical (100) peak located at ~12.87° was related to the in-plane arrangement of nitrogen-linked heterocyclic rings, while the 27.48° peak corresponds to the (002) stacking layered structure [42]. It was obvious that the lateral peak shifted to higher 2θ angles in DR-CNNS, indicating smaller stacking distance between nanosheets (Fig. 1B) [42]. As displayed in Fig. 1C, the peaks of DR- TiO_2 and DR-CNNS were clearly observed in all DDR-xCyT composites, and the intensity of peak (002) increased with

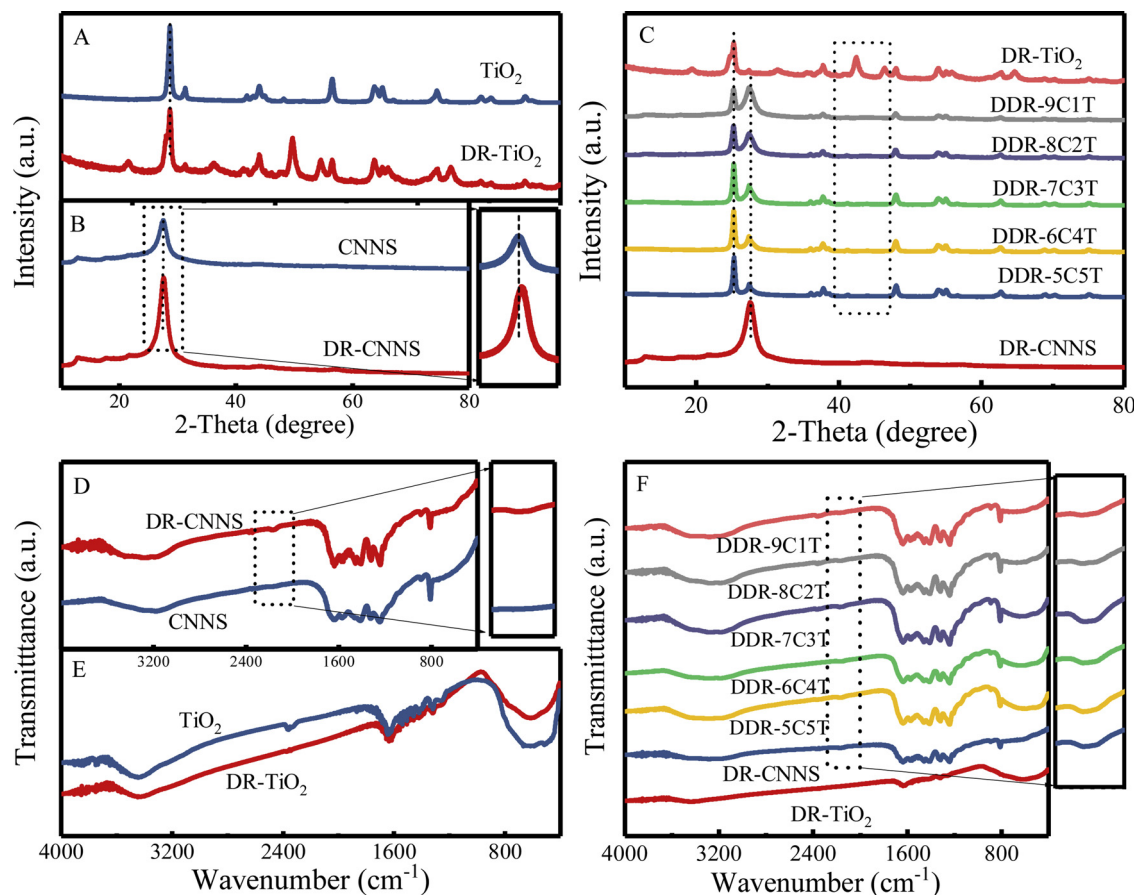


Fig. 1. (A–B) XRD patterns and (D–F) FTIR spectra of TiO_2 , CNNS, DR- TiO_2 , DR-CNNS and DDR- $x\text{CyT}$.

the increase of the mass of DR-CNNS. Interestingly, the characteristic peaks of pure TiO_2 became overwhelming in all DDR- $x\text{CyT}$ nanocomposites, while the peaks of several reduced TiO_2 (Ti_9O_{17} , Ti_8O_{15} and Ti_3O_5) almost disappeared. Although the underlying mechanism was still unclear, it could be concluded that CNNS had positive effect on the crystalline lattice deformation, demonstrating that our dual defective strategy did not alter the structure of the TiO_2 .

From FT-IR spectra (Fig. 1D), CNNS and DR-CNNS presented the basic characteristic peaks of $\text{g-C}_3\text{N}_4$. The band at $\sim 808 \text{ cm}^{-1}$ was assigned to tri-s-triazine unit mode [53]. Meanwhile, several vibration bands at $1200\text{--}1640 \text{ cm}^{-1}$ belong to the stretching vibrations of aromatic CN heterocycles [54]. In addition, the band at $3000\text{--}3400 \text{ cm}^{-1}$ was attributed to the terminal amino groups and the hydroxyl group of the adsorbed H_2O . The results indicated that DR-CNNS maintained the core $\text{g-C}_3\text{N}_4$ heterocycle structure similar to CNNS. Furthermore, the new vibration band at $\sim 2175 \text{ cm}^{-1}$ was observed, indicating the formation of terminal cyano functional groups [27,42,55]. For the spectra of TiO_2 and DR- TiO_2 (Fig. 1E), the peak at $\sim 400\text{--}900 \text{ cm}^{-1}$ could be assigned to Ti-O-Ti and Ti-O stretching vibration [25], and the other two peaks at ~ 1635 and $\sim 3400\text{--}3500 \text{ cm}^{-1}$ were corresponding to $-\text{OH}$ and the absorbed H_2O . For composites, the peaks at $\sim 808 \text{ cm}^{-1}$ and $\sim 1200\text{--}1640 \text{ cm}^{-1}$ were corresponding to the characteristic stretching modes of $\text{g-C}_3\text{N}_4$ in the DDR- $x\text{CyT}$ (Fig. 1F), indicating the presence of DR-CNNS. Moreover, the absorption peaks in the range of $\sim 400\text{--}900 \text{ cm}^{-1}$ were related to the existence of TiO_2 . In addition, the peaks at $\sim 2175 \text{ cm}^{-1}$, attributing to the terminal cyano functional group, could be identified in the hybrids, which confirmed that a hybrid was successfully formed from DR- TiO_2 and DR-CNNS.

As shown in Fig. 2A, DR-CNNS had a wrinkle sheet-like and hierarchical structure similar to pristine $\text{g-C}_3\text{N}_4$ nanosheets (Figure S1). The HRTEM image (Fig. 2B) displayed a huge amount of random disorder in

the basal plane domain of DR-CNNS. As shown in Fig. 2C, the average diameter of DR- TiO_2 was $\sim 20\text{--}40 \text{ nm}$, no obvious crystal sizes change of pristine TiO_2 was detected during the treatment (Figure S2). The HRTEM image (Fig. 2D) revealed that obvious disordered surface layer ($\sim 2\text{--}3 \text{ nm}$) could be observed due to the reconstructed oxygen vacancy layer. Furthermore, the DR- TiO_2 particles were dispersed randomly on the DR-CNNS in DDR-7C3T (Fig. 2E), meanwhile, the particle size of DR- TiO_2 had no significant change. Some DR- TiO_2 particles were also wrapped by DR-CNNS nanosheets because $\text{g-C}_3\text{N}_4$ is a soft polymer. Moreover, no scattered particles can be observed from the outside of DR-CNNS in the TEM images, suggesting the intimate interaction between DR-CNNS and DR- TiO_2 . An apparent heterointerfaces were also observed between DR- TiO_2 and DR-CNNS (Fig. 2F–H). The lattice fringes of the crystalline core were 0.35 nm , belonging to the lattice plane (101) of anatase TiO_2 [13], while the lattice fringes of DR-CNNS cannot be observed due to its weak crystallinity [56,57]. Further, the elemental mappings (Fig. 2I–M) displayed the homogeneous distribution of C, N, O and Ti elements in the DDR-7C3T. These results also indirectly indicated that DR- TiO_2 was successfully incorporated with the DR-CNNS.

The chemical compositions and states were further investigated by XPS. As shown in Fig. 3A, the XPS survey spectrum indicated the presence of C, N, Ti and O in DDR-7C3T composite. For C 1s spectra of as-prepared samples (Fig. 3B), the peaks at $\sim 284.68 \text{ eV}$ could be ascribed to sp^2 C–C bonds of graphitic carbon, while the peak at $\sim 288.69 \text{ eV}$ belong to the sp^2 -bonded carbon ($\text{N}=\text{C}=\text{N}$) [27,58]. The peaks in N 1s region at ~ 397.23 , ~ 398.65 and $\sim 399.96 \text{ eV}$ were assigned to sp^2 hybridized N ($\text{C}=\text{N}=\text{C}$), ternary nitrogen groups ($\text{N}-(\text{C})_3$) and amino groups ($\text{C}-\text{N}-\text{H}$), respectively (Fig. 3C) [40,59]. Interestingly, compare to DR-CNNS, the N 1s core level spectrum of DDR-7C3T shifted to lower binding energy, implying the interface interaction formation between DR- TiO_2 and DR-

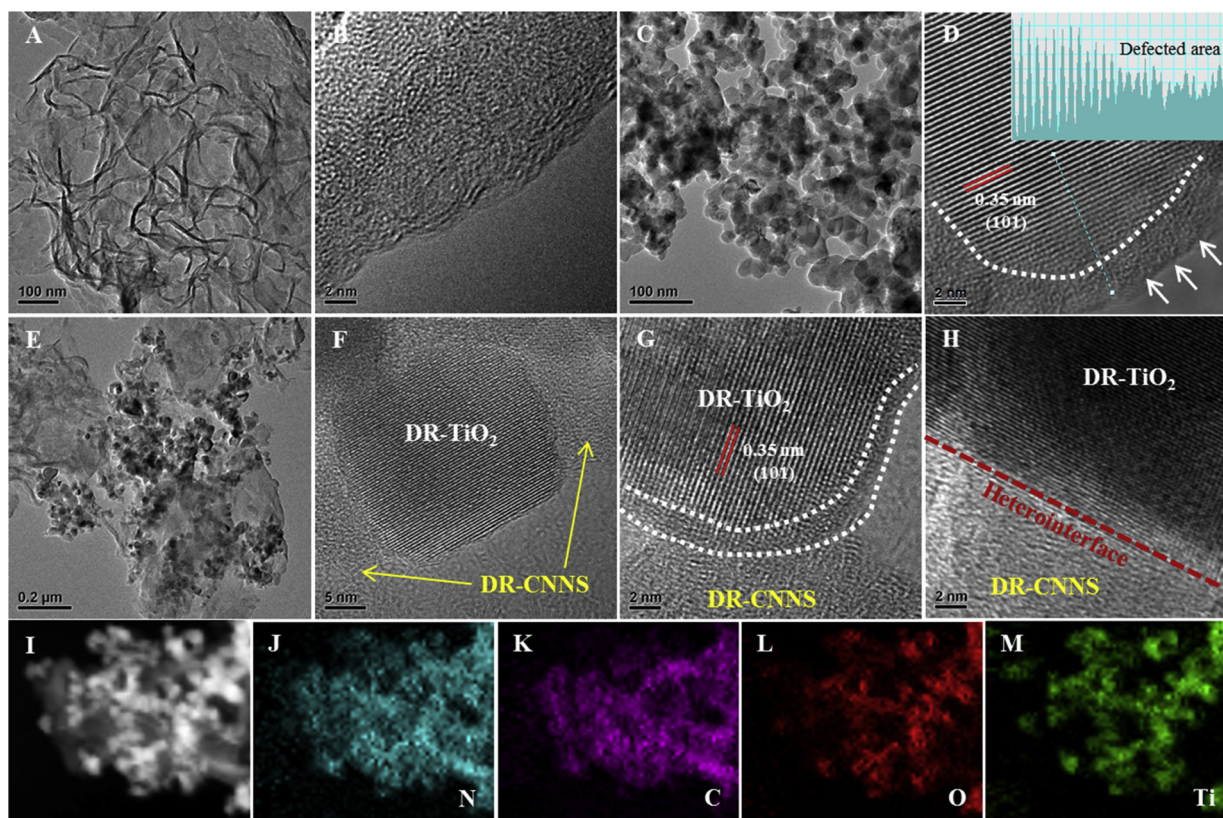


Fig. 2. (A–B) TEM and HRTEM images of DR-CNNS; (C–D) TEM and HRTEM images of DR-TiO₂ with line profile of the selected area; (E–H) TEM and HRTEM images of DDR-7C3T heterostructure; (I–M) Elemental mapping images of DDR-7C3T heterostructure.

CNNS in DDR-7C3T [25]. For Ti 2p, as shown in Fig. 3D, two peaks at ~458.18 and ~463.88 eV were related to the Ti⁴⁺ 2p_{3/2} and Ti⁴⁺ 2p_{1/2}, respectively, which were assigned to Ti⁴⁺ in TiO₂ [60]. For DR-TiO₂ and DDR-7C3T, two new peaks at ~456.97 and ~462.36 eV were assigned to the Ti³⁺ 2p_{3/2} and Ti³⁺ 2p_{1/2}, respectively, demonstrating the successful insertion of Ti³⁺ and/or oxygen defects into the TiO₂ lattice [7]. The up-shift of the Ti 2p peaks and the down-shift of the N 1s peaks confirmed that a novel DDR-7C3T heterojunction was successfully constructed between the interfaces, which would be expected to facilitate the photogenerated carriers separation and migration, thus enhancing the photocatalytic performance of the DDR-xCyT heterostructure. For O 1s spectra of TiO₂ (Fig. 3E), the peaks at ~530.13 and ~531.15 eV belonged to the Ti–O–Ti bond and adsorbed O₂, respectively. After NaBH₄ treatment, an emerging peak at ~532.85 eV belonged to Ti–OH bond was observed, meanwhile, the intensity of the Ti–OH peak of the DDR-7C3T increased compared with DR-TiO₂, which is attributed to the fact that more defect sites are easily combined with hydrogen atoms to form more Ti–OH [11]. The increase in concentration of surface Ti–OH further improved the surface hydrophilicity of the DDR-7C3T, thus can greatly enhance the PHE activity. As a result, it could be concluded that oxygen defects were successfully introduced into DDR-7C3T. Meanwhile, the binding energy shifts of the Ti 2p peaks and N 1s peaks for the heterojunction material manifested the intimate interfacial contact and strong interactions between DR-CNNS and DR-TiO₂, which was crucial for the formation of effective heterojunctions. Furthermore, ESR measurement was employed to study the defects in photocatalysts, as shown in Fig. 3F. Both CNNS and DR-CNNS exhibited one single Lorentzian line in a magnetic field from 3500 to 3600 G, which was caused by unpaired electrons on carbon atoms of the aromatic rings. DR-CNNS showed a significantly enhanced peak intensity as compared to CNNS due to the π-electron redistribution caused by the –C≡N group. Furthermore, TiO₂ showed no obvious ESR signal, while DR-TiO₂ exhibited a sharp ESR signal, which was

characteristic of oxygen defect. For DDR-7C3T, the ESR response was lower than that of DR-CNNS due to the vacancy structure of DR-CNNS being sewed up at a certain degree by the DR-TiO₂. Combined with the XPS results, it could be concluded that the dual defect was successfully formed in DDR-7C3T. The rich dual defect could significantly affect its optical properties and electronic structures of the DDR-xCyT.

The optical properties were investigated by UV-vis DRS (Fig. 4A). Both TiO₂ and CNNS exhibited sharp absorption band edges at ~386 and ~450 nm. After NaBH₄ treatment, DR-TiO₂ displayed a broad adsorption in visible light and further extended to the near infrared region. The adsorption band intensity of DR-TiO₂ increased dramatically, which was consistent with the color change of as-prepared samples (Figure S3). The absorption edge of CNNS was ~447 nm, while the absorption edge of the DR-CNNS possesses red-shifted in comparison with CNNS, which enables the extended light adsorption due to the introduced defects. It was noticeable that the DDR-xCyT had stronger visible light response and obviously red-shifted absorption edge. According to Mott–Schottky results (Figure S4), both DR-TiO₂ and DR-CNNS are n-type semiconductors [61,62]. As we known, there is no band gap for composites, so we only studied the band structure of DR-TiO₂ and DR-CNNS. The corresponding E_g values were ~2.74, ~2.66, ~3.21 and ~2.48 eV for CNNS, DR-CNNS, TiO₂ and DR-TiO₂, respectively (Fig. 4B). The reduced E_g value of DR-TiO₂ (~2.48 eV) vs. pristine TiO₂ (~3.21 eV) was due to the introduced defects [63]. The red-shifted absorption edge in DR-CNNS presented a reduced E_g value of ~2.66 eV (Fig. 4B), implying that the combination of DR-CNNS with DR-TiO₂ could produce more photocatalytic electrons and promote the PHE activity. The valence band (VB) position was further analyzed through VB XPS spectra (Fig. 4C). The VB XPS of CNNS, DR-CNNS, TiO₂, and DR-TiO₂ showed the position of VB top at ~–1.28, ~–1.22, ~–0.54 and ~–0.06 eV, respectively, indicating the efficient band engineering. Combining with the above results, the band structures of samples were well resolved, as illustrated in Fig. 4D. This upward shift of the VB and the downward

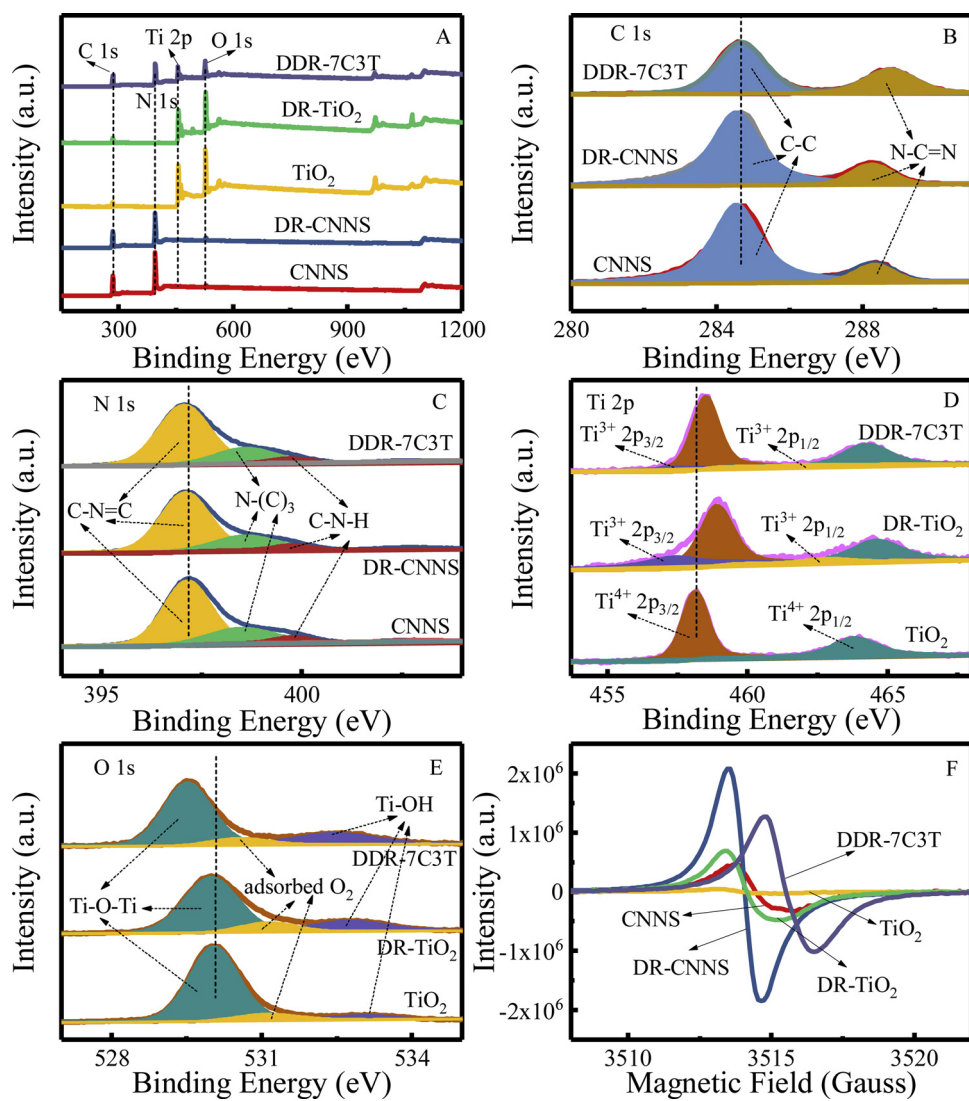


Fig. 3. XPS spectra of (A) survey for TiO_2 , CNNS, DR- TiO_2 , DR-CNNS and DDR-7C3T; (B) C 1s and (C) N 1s in CNNS DR-CNNS and DDR-7C3T; (D) Ti 2p and (E) O 1s in TiO_2 , DR- TiO_2 and DDR-7C3T; (F) EPR spectra of TiO_2 , CNNS, DR- TiO_2 , DR-CNNS and DDR-7C3T.

shift of the conduction band (CB) were due to the presence of defects. It was concluded that the defect strategy is an effective method to modify the band structure of $\text{g-C}_3\text{N}_4$ and TiO_2 .

H_2 evolution reaction was carried out to evaluate the photocatalytic performance of photocatalysts. Effect of the amount of photocatalyst on photocatalytic hydrogen evolution was investigated (Figure S5). It can be seen that the H_2 evolution rate increased, and eventually plateaued at ≥ 10 mg. The mass is greater than 10 mg, and the photocatalytic activity is no longer increased due to the negative influence of excess photocatalyst on light absorption. Therefore, 10 mg of photocatalyst was used in the next photocatalytic tests. As shown in Fig. 5A,B, DR-CNNS showed a HER of $\sim 242.11 \mu\text{mol}/\text{h}$, higher than that of CNNS ($\sim 134.18 \mu\text{mol}/\text{h}$), corroborating the benefits of abundant defective structures within the light harvester. However, DR- TiO_2 showed very low activity ($\sim 28.1 \mu\text{mol}/\text{h}$), which might be due to the fact that the CB of DR- TiO_2 was too close to the potential of water reduction to drive excited electrons for H_2 evolution reaction. As expected, DR- TiO_2 /CNNS and TiO_2 /DR-CNNS showed higher H_2 evolution rate of ~ 293.48 and $\sim 368.59 \mu\text{mol}/\text{h}$, respectively, suggesting that the heterostructure played an effective role in increasing the photocatalytic activity. More significantly, the coupling of DR-CNNS with DR- TiO_2 indeed led to a significant increase in PHE activity. The optimized DDR-7C3T presented the highest PHE rate of $\sim 651.79 \mu\text{mol}/\text{h}$, which was ~ 2.7 and

~ 23.3 times that of DR-CNNS and DR- TiO_2 , respectively. The corresponding apparent quantum yield could reach up to $\sim 4.45\%$ at 420 nm. These results were related to its dual defective structure, heterojunction and intimate interfacial contact. Notably, the H_2 evolution rate of DDR-7C3T was notably higher than that of most $\text{g-C}_3\text{N}_4$ -based photocatalysts reported previously (Table S1). Moreover, the relative content of DR-CNNS with DR- TiO_2 influenced the photocatalytic activity of the DDR- xCyT (Fig. 5C,D). All DDR- xCyT exhibited higher PHE activities than the pristine DR-CNNS and DR- TiO_2 . The PHE activity first increased and then decreased with the increment of DR- TiO_2 in composites. The excess amount of DR- TiO_2 would cover the reaction sites on the DR-CNNS surface, hindering the reduction of H^+ into H_2 . The much narrower band-gap DR- TiO_2 might act as a recombination center, thus inhibiting photocatalytic performance [64]. Although DR- TiO_2 showed the highest photo absorption, it had the lowest catalytic activity, which further indicated that light utilization was not the only factor affecting PHE. Meanwhile, the dual defective structured DDR- xCyT had much higher activity than DR- TiO_2 /CNNS and TiO_2 /DR-CNNS. These results discussed above indicated that the dual defective structure dramatically influenced the photocatalytic performances of composites. Furthermore, the PHE rate of DDR-7C3T also far exceeds that of most other $\text{g-C}_3\text{N}_4$ - and TiO_2 -based photocatalysts in previous literatures (Figure S6), further confirming that the rationally designed dual defect structure is

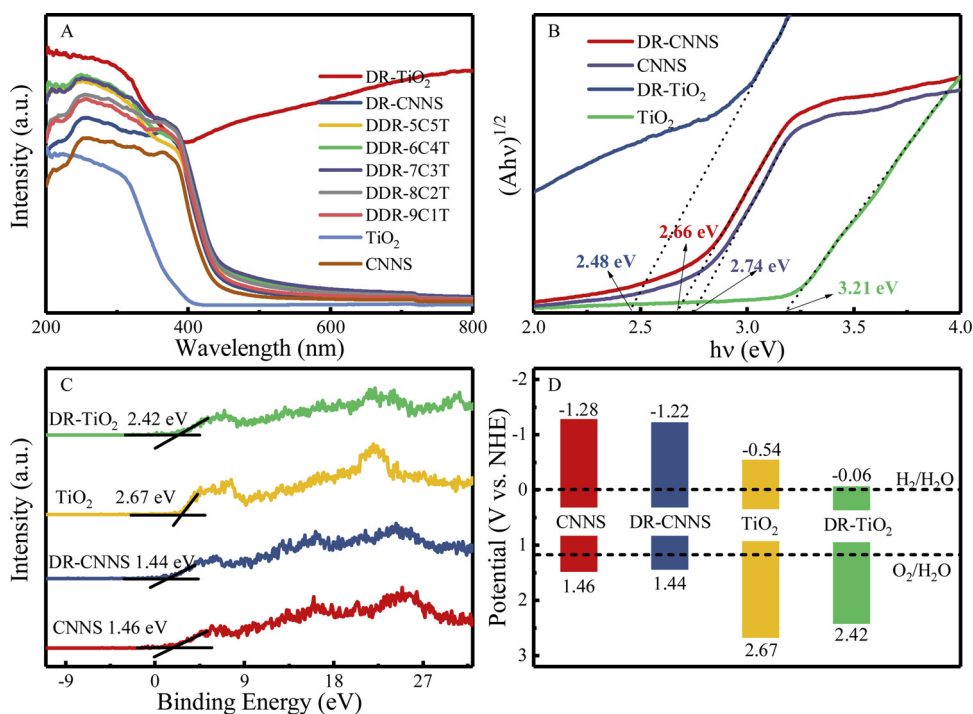


Fig. 4. (A) UV-vis DRS spectra of TiO₂, CNNS, DR-TiO₂, DR-CNNS and DDR-xCyt; (B) The corresponding Tauc plots of $(\text{d}\text{h}\nu)^{1/2}$ versus $\text{h}\nu$ of TiO₂, CNNS, DR-TiO₂, DR-CNNS; (C) VB XPS and (D) band energy diagram of TiO₂, CNNS, DR-TiO₂ and DR-CNNS.

the potential strategy for preparing high efficiency photocatalysts. Dual defect could act not only as photogenerated charge traps, promoting photogenerated electrons separation and transfer, but also provide more active sites where the photogenerated electrons transferred to the H⁺, and thus significantly improving PHE activity [65].

UV-vis DRS and wavelength-dependent PHE were measured to understand the photocatalytic process on DDR-7C3T heterostructures (Fig. 6A). DDR-7C3T presented a high H₂ evolution rate in a range of ~400–450 nm, the variation tendencies of rate curves were similar to their UV/Vis light absorption spectra. This improved photocatalytic

performance of DDR-7C3T should be attributed to the narrowed band gap from the dual defective structure and the heterojunction prompted photocatalytic charge separation and transfer. The turnover frequency (TOF) of DDR-7C3T reached ~419.3 h⁻¹, which was ~4.91 and ~7.07 times that of CNNS and TiO₂, respectively (Fig. 6B). As shown in Fig. 6C, after irradiating for 12 h, DDR-7C3T hybrid produced ~7.79 × 10³ μmol H₂ gas and kept proportional increase to time, indicating the high photocatalytic stability of DDR-7C3T heterostructure. The photocatalytic activity of DR-CNNS + DR-TiO₂ was also tested and presented in Fig. 6D. It should be noted that DR-CNNS + DR-TiO₂

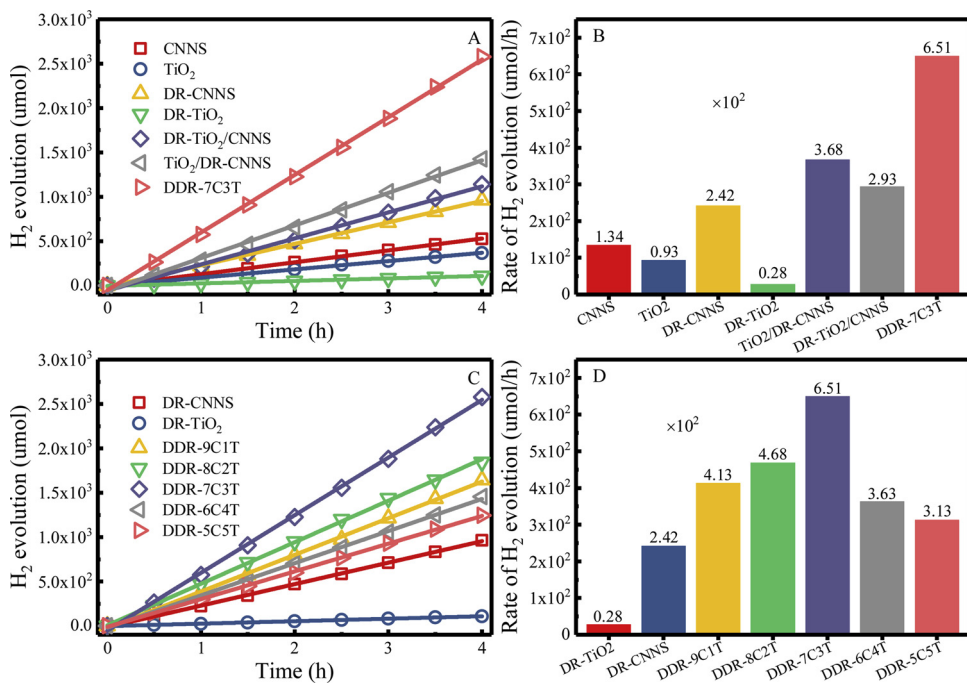


Fig. 5. (A and C) Photocatalytic H₂ evolution performances and (B and D) evolution rate of different photocatalysts.

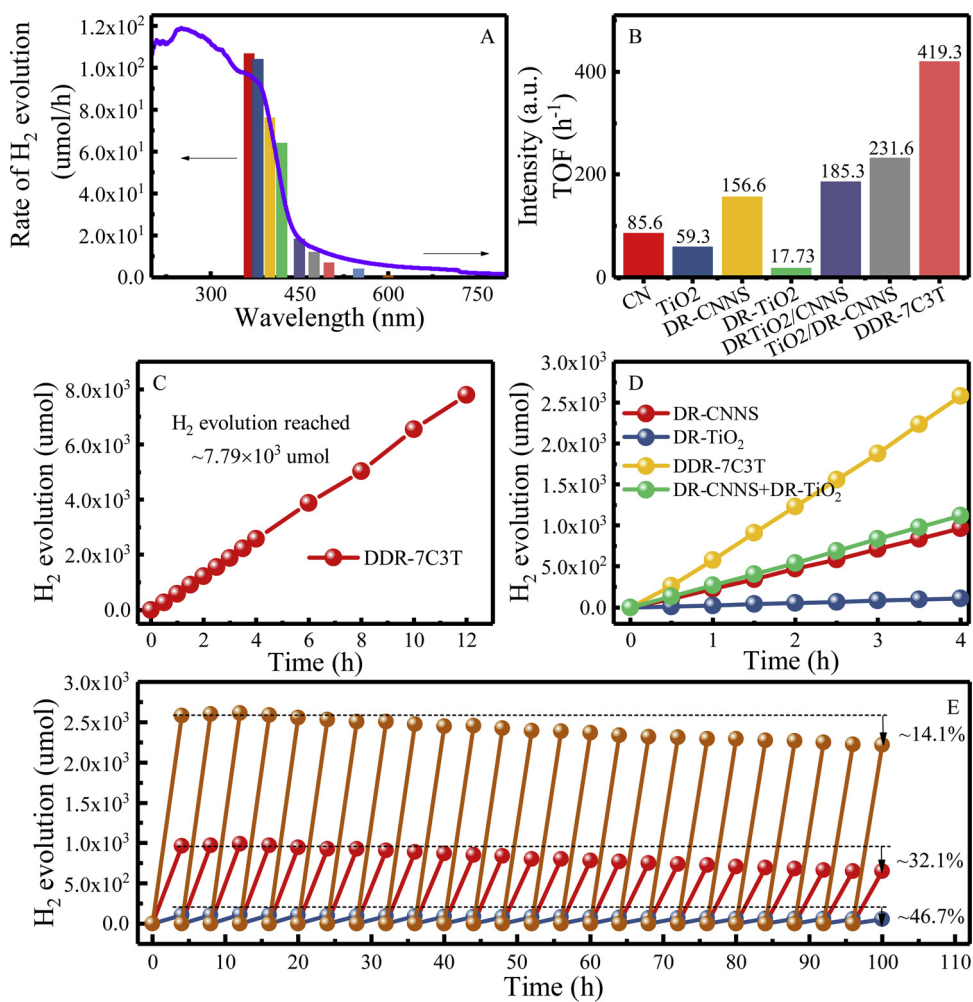


Fig. 6. (A) Wavelength dependent H_2 evolution rate and UV-vis DRS spectra of DDR-7C3T; (B) Turnover frequency of different photocatalysts; (C) Photocatalytic stability of DDR-7C3T; (D) Photocatalytic H_2 evolutions of DR-CNNS + DR-TiO₂; (E) Cycling test of photocatalytic H_2 evolution for DR-CNNS, DR-TiO₂ and DDR-7C3T.

yielded $\sim 1.12 \times 10^3$ μmol H_2 gas, which was lower than that of DDR-7C3T. This could be attributed to the weak contact between DR-CNNS and DR-TiO₂, resulting in the decelerated migration of photogenerated charges at the interface [66]. The photocatalytic stabilities of DR-CNNS, DR-TiO₂ and DDR-7C3T were further evaluated by recycling experiments (Fig. 6E). Notably, the H_2 evolution activity of DDR-7C3T remained relatively high stability after 100 h test. The results demonstrated that DDR-7C3T was a highly efficient catalyst for PHE reactions [67]. However, the recycling experiments of DR-CNNS and DR-TiO₂ presented poor stability with an obvious deactivation activity (~32.1% and ~46.7%) after 100 h tests. These results confirmed that the dual defective structure could not only boost PHE performance, but also improve the stability of photocatalysts [68].

To get insight into the catalytic mechanism, spectroscopic and photoelectrochemical studies were conducted. As revealed in Fig. 7A, the transient photocurrent ($i-t$) curves showed that DDR-7C3T could deliver an evidently strengthened photocurrent response than the DR-TiO₂/CNNS and TiO₂/DR-CNNS, indicating the remarkably increased separation and migration efficiency of photogenerated charge due to the dual defective structure in composite. Meanwhile, the electrochemical impedance spectroscopy (EIS) results indicated that the DDR-7C3T hybrid displayed a smaller semicircle in the Nyquist plots than that of the DR-TiO₂/CNNS and TiO₂/DR-CNNS (Fig. 7B), indicating that electrons can be easily transferred to the protons in the electrolyte [69]. Moreover, the steady-state PL intensity of DDR-7C3T was lowest, which

indicated that dual defects could remarkably affect the lifetime of the photogenerated charge (Fig. 7C). That is, the suppression of PL implies either slower recombination (longer lifetime of the photogenerated electrons) or faster transfer (shorter decay lifetime of the photogenerated electrons) [70,71]. To gain more information on this, TRPL spectra were further employed to characterize the lifetime of photogenerated charge. In Fig. 7D, the decay curves was fitted by the following equation [72–75]:

$$I(t) = A + B_1 \left(-\frac{t}{\tau_1} \right) + B_2 \left(-\frac{t}{\tau_2} \right)$$

where B_1 and B_2 are the pre-exponential functions. The τ_1 and τ_2 is the surface-related nonradiative recombination processes and the recombination of free excitons, respectively. The intensity-average lifetime τ was calculated by the following the equation [72–75]:

$$\tau = \frac{B_1 \tau_1^2 + B_2 \tau_2^2}{B_1 \tau_1 + B_2 \tau_2}$$

The results indicated that the τ_1 and τ_2 of the DDR-7C3T are longer than the corresponding values of the DR-TiO₂/CNNS and TiO₂/DR-CNNS, respectively. Meanwhile, DDR-7C3T showed the longest lifetime ($\tau = 4.227$ ns), while TiO₂/DR-CNNS presented a shorter lifetime ($\tau = 3.461$ ns), followed by DR-TiO₂/CNNS ($\tau = 3.125$ ns). Therefore, the results confirmed that the lifetimes of charge carriers in DDR-7C3T are lengthened by the dual defective structure. Accordingly, the

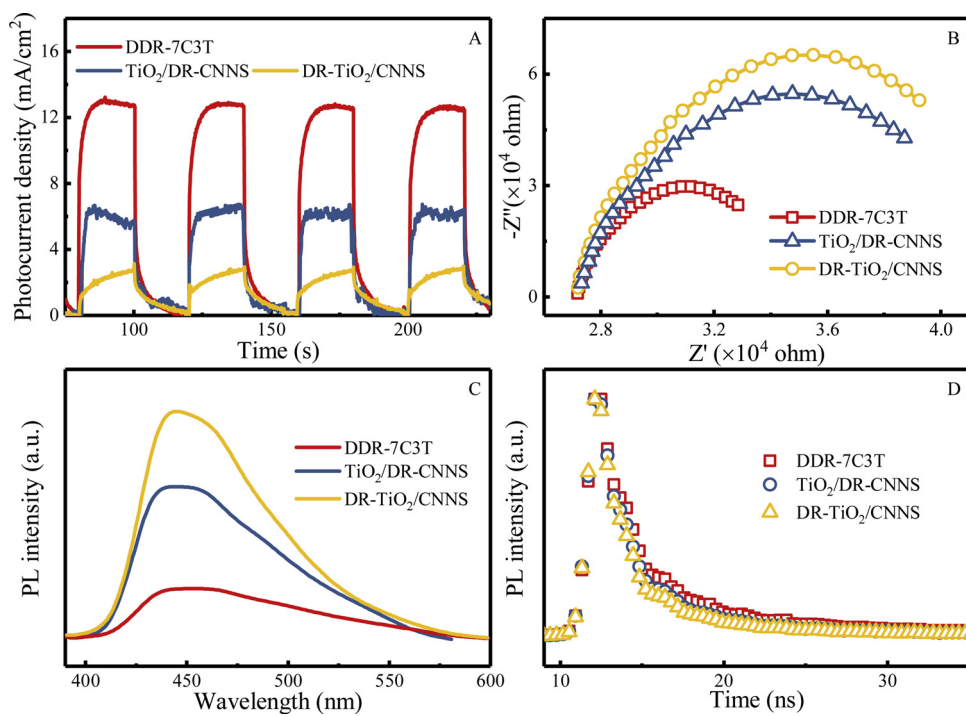


Fig. 7. (A) i-t curves (B) EIS Nyquist plots, (C) Room-temperature PL and (D) TRPL spectra of TiO₂/DR-CNNS, DR-TiO₂/CNNS and DDR-7C3T.

prolonged lifetimes of photogenerated electrons combined the quenched PL intensity should be ascribed to the effectively suppressive recombination of photogenerated charge due to the "electron trapping" process based on the "Z-scheme" mechanism, resulting in a promoted photocatalytic activity for H₂ evolution [76–78]. All above results confirmed that the existence of dual defective heterostructure and the interfacial contact formed between DR-TiO₂ and DR-CNNS. It facilitated the transportation and separation of photogenerated charges, improving the PHE performance.

To validate the Z-scheme mechanism, we used DMPO spin-trapping ESR spectrum to study the formation of ·OH and ·O₂[−] radicals for DDR-7C3T (Fig. 8A,B). Negligible ESR signals were observed under dark conditions. However, the obvious DMPO-·O₂[−] signals were observed in DDR-7C3T, whereas the DMPO-·O₂[−] signals can hardly be detected in DR-TiO₂ (Fig. 8A) [79]. Meanwhile, the intensity of DMPO-·O₂[−] in DDR-7C3T was much stronger than that of DR-CNNS, which can be ascribed to the improved photogenerated charge separation and migration efficiency. As shown in Fig. 8B, the typical DMPO-·OH spin adduct possessed a characteristic 1:2:2:1 quadrupole were observed in DR-TiO₂ and DDR-7C3T, while no signal was detected over DR-CNNS [80]. The coexistence of ·O₂[−] and ·OH radicals confirmed that the photogenerated charge separation mechanism is the Z-scheme mechanism rather than the traditional type-II heterojunction [44,81]. Moreover, the intensity of both DMPO-·O₂[−] and DMPO-·OH signals over the DDR-7C3T was stronger than those of DR-CNNS and DR-TiO₂, indicating that the Z-scheme system was more conducive to the separation and transfer of photogenerated charges. Moreover, terephthalic acid (TA) was further used as a probe molecule to examine the ·OH production over the DDR-7C3T. As shown in Fig. 8C, the PL intensity at ~426 nm gradually increased with increasing irradiation time during the photocatalytic reaction, which indicated the gradual production of ·OH [68]. This revealed that the photocatalytic mechanism of DDR-7C3T heterostructure was based upon the Z-scheme heterojunction.

The photocatalytic mechanisms in the DDR-7C3T heterostructure could be elucidated with the help of two possible charge separation ways i.e. the traditional type-II charge separation mechanism and Z-scheme mechanism (Fig. 8D). Based on the band structure analysis

(Fig. 4), the CB potentials of DR-TiO₂ and DR-CNNS were −0.06 and −1.22 eV, respectively, and the VB positions were +2.42 and +1.44 eV, respectively. As shown in Fig. 8D-(a), the electrons in the CB of DR-CNNS would migrate to the CB of DR-TiO₂ provided the formation of DR-TiO₂ and DR-CNNS as type-II heterojunction. Meanwhile, the holes on the VB of DR-TiO₂ would transfer to the VB of DR-CNNS. As a result, the electrons accumulated to the CB of DR-TiO₂ and the holes in the VB of DR-CNNS were well separated from each other. If so, the electrons on the CB of DR-TiO₂ could not reduce O₂ to generate ·O₂[−] due to the CB potential of DR-TiO₂ was more positive than that of O₂/O₂[−] (−0.33 V). At the same time, the holes of DR-CNNS could not oxidize H₂O to give ·OH owing to the more negative than that of ·OH (+1.99 V). Nevertheless, the ESR results indicated that both ·O₂[−] and ·OH were the active species. Apparently, traditional type-II charge separation mechanism was not suitable for the DDR-7C3T system. According to the above results and discussion, the Z-scheme heterojunction was proposed (Fig. 8D-(b)). Under light irradiation, the CB electrons in DR-TiO₂ would transfer and recombine with the VB holes in DR-CNNS, following the Z-scheme pathway, thus maintaining the strong electron reducibility of DR-CNNS CB and strong holes oxidizability of DR-TiO₂ VB, generating abundant ·O₂[−] and ·OH, which were in agreement with the ESR analysis. Then the electrons of DR-CNNS CB would gather on the surface of Pt co-catalysts, and interact with the H⁺ to H₂ evolution.

Importantly, this method is rather general and can be also used to prepare other double defective heterojunctions, such as DR-ZnO/DR-CNNS and DR-SnO₂/DR-CNNS, etc. The optical absorption of DR-ZnO/DR-CNNS and DR-SnO₂/DR-CNNS were measured, showing greatly enhanced absorption due to the introduced dual defects (Figure S7). Photocatalytic H₂ production activity over different dual defective photocatalysts was also evaluated. As shown in Figure S8, all of dual defective heterojunctions exhibited considerably enhanced PHE activities, such as the PHE rate of ~1.72 × 10² μmol/h for DR-SnO₂/DR-CNNS. This exciting finding clearly showed an enormous potential in coupling defective g-C₃N₄ with a wide variety of defective oxide photocatalysts to form a double-pitched heterostructure.

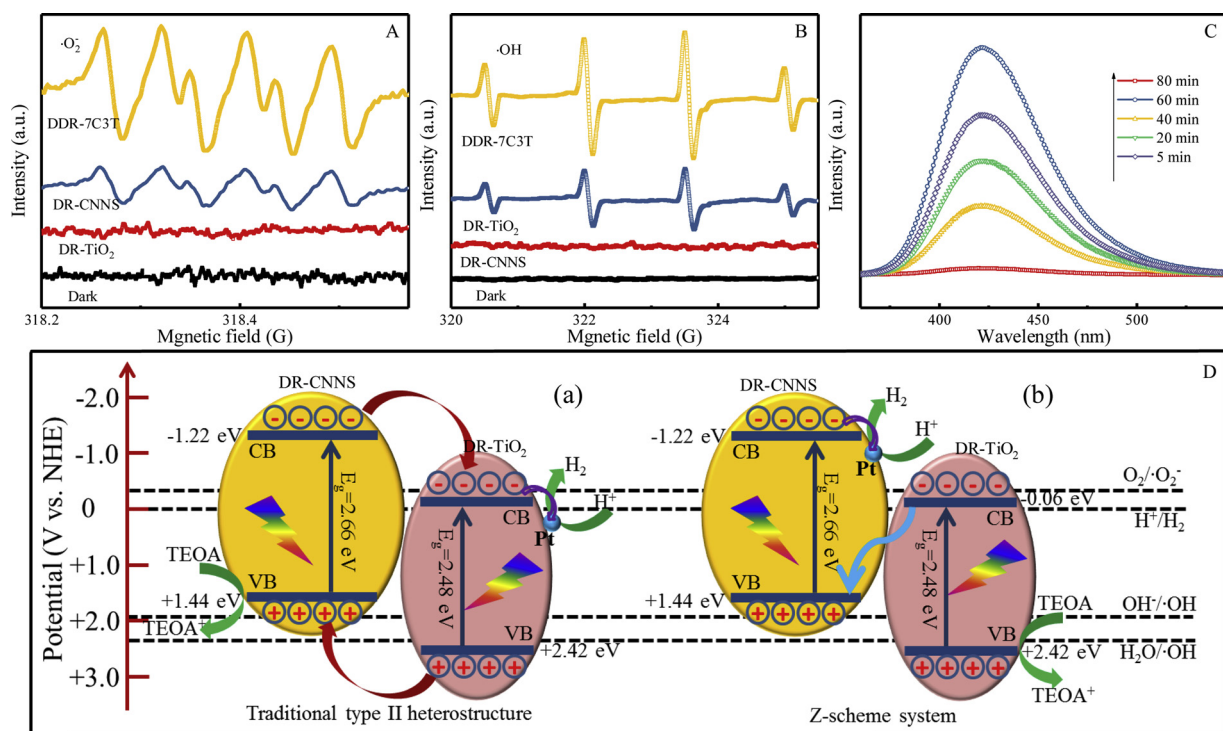


Fig. 8. DMPO spin-trapping ESR spectra recorded for (A) $\cdot\text{O}_2^-$ and (B) $\cdot\text{OH}$ under visible light for DR-CNNS, DR-TiO₂ and DDR-7C3T; (C) Fluorescence intensity of $\cdot\text{OH}$ -trapping PL spectra of the DDR-7C3T; (D) Schematic diagram for the possible charge separation and transfer mechanisms of DDR-7C3T.

4. Conclusions

In summary, we have designed and fabricated, for the first time, dual defective heterojunctions between defect-rich g-C₃N₄ and defect-rich oxide materials. XPS, ESR and UV-vis DRS revealed that the presence of abundant defects in the DDR-7C3T led to the narrowed band gap and extended light spectral response. The binding energy shifts of the Ti 2p peaks and N 1s peaks confirmed that intimate interface was successfully constructed between the interfaces, consequently facilitating faster electron transfer across the interface and elongate the lifetimes of charge carriers, which were confirmed by electrochemical analysis and PL/TRPL spectra. The optimized DDR-xCyT showed superior hydrogen evolution rate of $\sim 651.79 \mu\text{mol}/\text{h}$ with a turnover frequency of $\sim 419.3 \text{ h}^{-1}$, as well as stability and recyclability, which was higher than previously reported defective TiO₂ or g-C₃N₄-based photocatalysts. The resulting $\cdot\text{O}_2^-$ and $\cdot\text{OH}$ further proved that the photogenerated charge separation mechanism followed Z-scheme mechanism. This protocol could be extended to prepare other dual defective g-C₃N₄/oxides (ZnO, SnO₂, etc). The present study is anticipated to provide novel insights for rational design and preparation of Z-scheme catalyst using defect engineering.

Acknowledgements

The work was financially supported by National Natural Science Foundation of China (Grant No. 21707043, 21876178, 21677146), the Natural Science Foundation of Shandong Province (Grant No. ZR2017BEE005), the Jiangsu Provincial Key Laboratory of Radiation Medicine and Protection and the Priority Academic Program Development of Jiangsu Higher Education Institutions are acknowledged.

Appendix A. Supplementary data

Supplementary material related to this article can be found, in the online version, at doi:<https://doi.org/10.1016/j.apcatb.2019.01.004>.

References

- J. Ran, G. Gao, F.-T. Li, T.-Y. Ma, A. Du, S.-Z. Qiao, Ti₃C₂ MXene co-catalyst on metal sulfide photo-absorbers for enhanced visible-light photocatalytic hydrogen production, *Nat. Commun.* 8 (2017) 13907.
- W.J. Ong, L.L. Tan, Y.H. Ng, S.T. Yong, S.P. Chai, Graphitic carbon nitride (g-C₃N₄)-based photocatalysts for artificial photosynthesis and environmental remediation: are we a step closer to achieving sustainability? *Chem. Rev.* 116 (2016) 7159–7329.
- W. Xu, Y. Bai, Y. Yin, Surface engineering of nanostructured energy materials, *Adv. Mater.* 0 (2018) 1802091.
- W. Zhou, H. Fu, Defect-mediated electron–hole separation in semiconductor photocatalysis, *Inorg. Chem. Front.* 5 (2018) 1240–1254.
- X. Liu, G. Zhu, X. Wang, X. Yuan, T. Lin, F. Huang, Progress in black Titania: a new material for advanced photocatalysis, *Adv. Energy Mater.* 6 (2016) 1600452.
- X. Cai, L. Mao, S. Yang, K. Han, J. Zhang, Ultrafast charge separation for full solar spectrum-activated photocatalytic H₂ generation in a black Phosphorus–Au–CdS heterostructure, *ACS Energy Lett.* 3 (2018) 932–939.
- G. Ou, Y.S. Xu, B. Wen, R. Lin, B.H. Ge, Y. Tang, Y.W. Liang, C. Yang, K. Huang, D. Zu, R. Yu, W.X. Chen, J. Li, H. Wu, L.M. Liu, Y.D. Li, Tuning defects in oxides at room temperature by lithium reduction, *Nat. Commun.* 9 (2018) 1302.
- S. Bai, N. Zhang, C. Gao, Y. Xiong, Defect engineering in photocatalytic materials, *Nano Energy* 53 (2018) 296–336.
- X. Jiao, Z. Chen, X. Li, Y. Sun, S. Gao, W. Yan, C. Wang, Q. Zhang, Y. Lin, Y. Luo, Y. Xie, Defect-mediated electron–hole separation in one-unit-cell ZnIn₂S₄ layers for boosted solar-driven CO₂ reduction, *J. Am. Chem. Soc.* 139 (2017) 7586–7594.
- G. Ye, Y. Gong, J. Lin, B. Li, Y. He, S.T. Pantelides, W. Zhou, R. Vajtai, P.M. Ajayan, Defects engineered monolayer MoS₂ for improved hydrogen evolution reaction, *Nano Lett.* 16 (2016) 1097–1103.
- J.-J. Li, B. Weng, S.-C. Cai, J. Chen, H.-P. Jia, Y.-J. Xu, Efficient promotion of charge transfer and separation in hydrogenated TiO₂/WO₃ with rich surface-oxygen-vacancies for photodecomposition of gaseous toluene, *J. Hazard. Mater.* 342 (2018) 661–669.
- J. Chen, G. Wu, T. Wang, X. Li, M. Li, Y. Sang, H. Liu, Carrier step-by-step transport initiated by precise defect distribution engineering for efficient photocatalytic hydrogen generation, *ACS Appl. Mater. Interfaces* 9 (2017) 4634–4642.
- H. Tan, Z. Zhao, M. Niu, C. Mao, D. Cao, D. Cheng, P. Feng, Z. Sun, A facile and versatile method for preparation of colored TiO₂ with enhanced solar-driven photocatalytic activity, *Nanoscale* 6 (2014) 10216–10223.
- X. Pan, M.-Q. Yang, X. Fu, N. Zhang, Y.-J. Xu, Defective TiO₂ with oxygen vacancies: synthesis, properties and photocatalytic applications, *Nanoscale* 5 (2013) 3601–3614.
- A. Sinhamahapatra, J.-P. Jeon, J.-S. Yu, A new approach to prepare highly active and stable black titania for visible light-assisted hydrogen production, *Energy Environ. Sci.* 8 (2015) 3539–3544.
- L. Lin, J. Huang, X. Li, M.A. Abass, S. Zhang, Effective surface disorder engineering of metal oxide nanocrystals for improved photocatalysis, *Appl. Catal. B: Environ.*

203 (2017) 615–624.

[17] J. Li, X. Wu, W. Pan, G. Zhang, H. Chen, Vacancy-rich monolayer BiO_{2-x} as a highly efficient UV, visible, and near-infrared responsive photocatalyst, *Angew. Chemie Int. Ed. English* 57 (2018) 491–495.

[18] W.-T. Liu, B.-H. Wu, Y.-T. Lai, N.-H. Tai, T.-P. Perng, L.-J. Chen, Enhancement of water splitting by controlling the amount of vacancies with varying vacuum level in the synthesis system of $\text{SnO}_{2-x}/\text{In}_2\text{O}_{3-y}$ heterostructure as photocatalyst, *Nano Energy* 47 (2018) 18–25.

[19] F. Lei, Y. Sun, K. Liu, S. Gao, L. Liang, B. Pan, Y. Xie, Oxygen vacancies confined in ultrathin indium oxide porous sheets for promoted visible-light water splitting, *J. Am. Chem. Soc.* 136 (2014) 6826–6829.

[20] O. Elbanna, M. Fujitsuka, S. Kim, T. Majima, Charge carrier dynamics in TiO_2 mesocrystals with oxygen vacancies for photocatalytic hydrogen generation under solar light irradiation, *J. Phys. Chem. C* 122 (2018) 15163–15170.

[21] X. Chen, L. Liu, F. Huang, Black titanium dioxide (TiO_2) nanomaterials, *Chem. Soc. Rev.* 44 (2015) 1861–1885.

[22] X. Chen, L. Liu, P.Y. Yu, S.S. Mao, Increasing solar absorption for photocatalysis with black hydrogenated titanium dioxide nanocrystals, *Science* 331 (2011) 746–750.

[23] S.G. Ullatil, S.B. Narendranath, S.C. Pillai, P. Periyat, Black TiO_2 nanomaterials: a review of recent advances, *Chem. Eng. J.* 343 (2018) 708–736.

[24] W. Zhou, W. Li, J.-Q. Wang, Y. Qu, Y. Yang, Y. Xie, K. Zhang, L. Wang, H. Fu, D. Zhao, Ordered mesoporous black TiO_2 as highly efficient hydrogen evolution photocatalyst, *J. Am. Chem. Soc.* 136 (2014) 9280–9283.

[25] B. Tan, X. Ye, Y. Li, X. Ma, Y. Wang, J. Ye, Defective anatase TiO_{2-x} mesocrystal growth in situ on $\text{g-C}_3\text{N}_4$ Nanosheets: construction of 3D/2D Z-scheme heterostructures for highly efficient visible-light photocatalysis, *Chem. - Eur. J.* 24 (2018) 13311–13321.

[26] C. Marchal, T. Cottineau, M.G. Méndez-Medrano, C. Colbeau-Justin, V. Caps, V. Keller, $\text{Au}/\text{TiO}_2/\text{g-C}_3\text{N}_4$ nanocomposites for enhanced photocatalytic H_2 production from water under visible light irradiation with very low quantities of sacrificial agents, *Adv. Energy Mater.* 8 (2018) 1702142.

[27] P. Niu, M. Qiao, Y. Li, L. Huang, T. Zhai, Distinctive defects engineering in graphitic carbon nitride for greatly extended visible light photocatalytic hydrogen evolution, *Nano Energy* 44 (2018) 73–81.

[28] Q. Han, B. Wang, Y. Zhao, C. Hu, L. Qu, A Graphitic- C_3N_4 “Seaweed” architecture for enhanced hydrogen evolution, *Angew. Chemie Int. Ed. English* 127 (2015) 11595–11599.

[29] Y. Kang, Y. Yang, L.-C. Yin, X. Kang, G. Liu, H.-M. Cheng, An amorphous carbon nitride photocatalyst with greatly extended visible-light-Responsive range for photocatalytic hydrogen generation, *Adv. Mater.* 27 (2015) 4572–4577.

[30] C.J. Rhodes, Photocatalysts based on graphitic carbon nitride: some prospects for artificial photosynthesis and the remediation of environmental pollution, *Sci. Prog. UK* 100 (2017) 400–410.

[31] W. Xing, W. Tu, Z. Han, Y. Hu, Q. Meng, G. Chen, Template-induced high-crystalline $\text{g-C}_3\text{N}_4$ nanosheets for enhanced photocatalytic H_2 evolution, *ACS Energy Lett.* 3 (2018) 514–519.

[32] Y.-Y. Han, X.-L. Lu, S.-F. Tang, X.-P. Yin, Z.-W. Wei, T.-B. Lu, Metal-free 2D/2D heterojunction of graphitic carbon nitride/graphdiyne for improving the hole mobility of graphitic carbon nitride, *Adv. Energy Mater.* 8 (2018) 1702992.

[33] K. Wang, G.K. Zhang, J. Li, Y. Li, X.Y. Wu, 0D/2D Z-Scheme heterojunctions of bismuth tantalate quantum dots/ultrathin $\text{g-C}_3\text{N}_4$ nanosheets for highly efficient visible light photocatalytic degradation of antibiotics, *ACS Appl. Mater. Interfaces* 9 (2017) 43704–43715.

[34] H.G. Yu, P. Xiao, P. Wang, J.G. Yu, Amorphous molybdenum sulfide as highly efficient electron-cocatalyst for enhanced photocatalytic H_2 evolution, *Appl. Catal. B: Environ.* 193 (2016) 217–225.

[35] J. Lia, J. Wang, G.K. Zhang, Y. Li, K. Wang, Enhanced molecular oxygen activation of Ni^{2+} -doped BiO_{2-x} nanosheets under UV, visible and near-infrared irradiation: mechanism and DFT study, *Appl. Catal. B: Environ.* 234 (2018) 167–177.

[36] J. Lia, W.H. Zhao, J. Wang, S.X. Song, X.Y. Wu, G.K. Zhang, Noble metal-free modified ultrathin carbon nitride with promoted molecular oxygen activation for photocatalytic formaldehyde oxidation and DFT study, *Appl. Surf. Sci.* 458 (2018) 59–69.

[37] Y. Kang, Y. Yang, L.-C. Yin, X. Kang, L. Wang, G. Liu, H.-M. Cheng, Selective breaking of hydrogen bonds of layered carbon nitride for visible light photocatalysis, *Adv. Mater.* 28 (2016) 6471–6477.

[38] Q. Tay, P. Kanhere, C.F. Ng, S. Chen, S. Chakraborty, A.C.H. Huan, T.C. Sum, R. Ahuja, Z. Chen, Defect engineered $\text{g-C}_3\text{N}_4$ for efficient visible light photocatalytic hydrogen production, *Chem. Mater.* 27 (2015) 4930–4933.

[39] L. Shi, L. Yang, W. Zhou, Y. Liu, L. Yin, X. Hai, H. Song, J. Ye, Photoassisted construction of holey defective $\text{g-C}_3\text{N}_4$ photocatalysts for efficient visible-light-driven H_2O_2 production, *Small* 14 (2018) 1703142.

[40] Q. Tay, X. Wang, X. Zhao, J. Hong, Q. Zhang, R. Xu, Z. Chen, Enhanced visible light hydrogen production via a multiple heterojunction structure with defect-engineered $\text{g-C}_3\text{N}_4$ and two-phase anatase/brookite TiO_2 , *J. Catal.* 342 (2016) 55–62.

[41] Q. Liang, Z. Li, Z.-H. Huang, F. Kang, Q.-H. Yang, Holey graphitic carbon nitride nanosheets with carbon vacancies for highly improved photocatalytic hydrogen production, *Adv. Funct. Mater.* 25 (2015) 6885–6892.

[42] H. Yu, R. Shi, Y. Zhao, T. Bian, Y. Zhao, C. Zhou, G.I.N. Waterhouse, L.-Z. Wu, C.-H. Tung, T. Zhang, Alkali-assisted synthesis of nitrogen deficient graphitic carbon nitride with tunable band structures for efficient visible-light-driven hydrogen evolution, *Adv. Mater.* 29 (2017) 1605148.

[43] S. Zhang, H. Yang, H. Gao, R. Cao, J. Huang, X. Xu, One-pot synthesis of CdS irregular nanospheres hybridized with oxygen-incorporated defect-rich MoS_2 ultra-thin nanosheets for efficient photocatalytic hydrogen evolution, *ACS Appl. Mater. Interfaces* 9 (2017) 23635–23646.

[44] Z. Jiang, W. Wan, H. Li, S. Yuan, H. Zhao, P.K. Wong, A hierarchical Z-scheme $\alpha\text{-Fe}_2\text{O}_3/\text{g-C}_3\text{N}_4$ hybrid for enhanced photocatalytic CO_2 reduction, *Adv. Mater.* 30 (2018) 1706108.

[45] X. Jia, M. Tahir, L. Pan, Z.-F. Huang, X. Zhang, L. Wang, J.-J. Zou, Direct Z-scheme composite of CdS and oxygen-defected CdWO_4 : an efficient visible-light-driven photocatalyst for hydrogen evolution, *Appl. Catal. B: Environ.* 198 (2016) 154–161.

[46] L. Jiang, X. Yuan, G. Zeng, J. Liang, X. Chen, H. Yu, H. Wang, Z. Wu, J. Zhang, T. Xiong, In-situ synthesis of direct solid-state dual Z-scheme $\text{WO}_3/\text{g-C}_3\text{N}_4/\text{Bi}_2\text{O}_3$ photocatalyst for the degradation of refractory pollutant, *Appl. Catal. B: Environ.* 227 (2018) 376–385.

[47] X.Q. Hao, J. Zhou, Z.W. Cui, Y.C. Wang, Y. Wang, Z.G. Zou, Zn-vacancy mediated electron-hole separation in $\text{ZnS}/\text{g-C}_3\text{N}_4$ heterojunction for efficient visible-light photocatalytic hydrogen production, *Appl. Catal. B: Environ.* 229 (2018) 41–51.

[48] Q. Li, Y. Xia, C. Yang, K. Lv, M. Lei, M. Li, Building a direct Z-scheme heterojunction photocatalyst by ZnIn_2S_4 nanosheets and TiO_2 hollowspheres for highly-efficient artificial photosynthesis, *Chem. Eng. J.* 349 (2018) 287–296.

[49] Q. Xu, L. Zhang, J. Yu, S. Wageh, A.A. Al-Ghamdi, M. Jaroniec, Direct Z-scheme photocatalysts: principles, synthesis, and applications, *Mater. Today* (2018).

[50] J. Low, C. Jiang, B. Cheng, S. Wageh, A.A. Al-Ghamdi, J. Yu, A review of direct Z-Scheme photocatalysts, *Small Methods* 1 (2017) 1700080.

[51] H. Cheng, J. Hou, O. Takeda, X.-M. Guo, H. Zhu, A unique Z-scheme 2D/2D nanosheet heterojunction design to harness charge transfer for photocatalysis, *J. Mater. Chem. A Mater. Energy Sustain.* 3 (2015) 11006–11013.

[52] X. Hao, Z. Cui, J. Zhou, Y. Wang, Y. Hu, Y. Wang, Z. Zou, Architecture of high efficient zinc vacancy mediated Z-scheme photocatalyst from metal-organic frameworks, *Nano Energy* 52 (2018) 105–116.

[53] F.-Y. Tian, D. Hou, F. Tang, M. Deng, X.-q. Qiao, Q. Zhang, T. Wu, D.-S. Li, Novel $\text{Zn}_{0.8}\text{Cd}_{0.2}\text{S}@\text{g-C}_3\text{N}_4$ core-shell heterojunctions with a twin structure for enhanced visible-light-driven photocatalytic hydrogen generation, *J. Mater. Chem. A Mater. Energy Sustain.* 6 (2018) 17086–17094.

[54] J.-H. Zhang, Y.-J. Hou, S.-J. Wang, X. Zhu, C.-Y. Zhu, Z. Wang, C.-J. Li, J.-J. Jiang, H.-P. Wang, M. Pan, C.-Y. Su, A facile method for scalable synthesis of ultrathin $\text{g-C}_3\text{N}_4$ nanosheets for efficient hydrogen production, *J. Mater. Chem. A Mater. Energy Sustain.* (2018).

[55] G. Liu, G. Zhao, W. Zhou, Y. Liu, H. Pang, H. Zhang, D. Hao, X. Meng, P. Li, T. Kako, J. Ye, In situ bond modulation of graphitic carbon nitride to construct p-n homojunctions for enhanced photocatalytic hydrogen production, *Adv. Funct. Mater.* 26 (2016) 6822–6829.

[56] L. Liu, Y.H. Qi, J.R. Lu, S.L. Lin, W.J. An, Y.H. Liang, W.Q. Cui, A stable $\text{Ag}_3\text{PO}_4@\text{g-C}_3\text{N}_4$ hybrid core@shell composite with enhanced visible light photocatalytic degradation, *Appl. Catal. B: Environ.* 183 (2016) 133–141.

[57] J.Y. Zhang, Y.H. Wang, J. Jin, J. Zhang, Z. Lin, F. Huang, J.G. Yu, Efficient visible-light photocatalytic hydrogen evolution and enhanced photostability of core/shell $\text{CdS}/\text{g-C}_3\text{N}_4$ nanowires, *ACS Appl. Mater. Interfaces* 5 (2013) 10317–10324.

[58] D. Zhang, X. Han, T. Dong, X. Guo, C. Song, Z. Zhao, Promoting effect of cyano groups attached on $\text{g-C}_3\text{N}_4$ nanosheets towards molecular oxygen activation for visible light-driven aerobic coupling of amines to imines, *J. Catal.* 366 (2018) 237–244.

[59] F. Wei, Y. Liu, H. Zhao, X. Ren, J. Liu, T. Hasan, L. Chen, Y. Li, B.-L. Su, Oxygen self-doped $\text{g-C}_3\text{N}_4$ with tunable electronic band structure for unprecedentedly enhanced photocatalytic performance, *Nanoscale* 10 (2018) 4515–4522.

[60] Y. Wang, X. Liu, C. Zheng, Y. Li, S. Jia, Z. Li, Y. Zhao, Tailoring TiO_2 nanotube-interlaced graphite carbon nitride nanosheets for improving visible-light-driven photocatalytic performance, *Adv. Sci.* 5 (2018) 1700844.

[61] G.L. Zhu, H. Yin, C.Y. Yang, H.L. Cui, Z. Wang, J.J. Xu, T.Q. Lin, F.Q. Huang, Black titania for superior photocatalytic hydrogen production and photoelectrochemical water splitting, *ChemCatChem* 7 (2015) 2614–2619.

[62] J.Y. Liu, W.J. Fang, Z.D. Wei, Z. Qin, Z. Jiang, W.F. Shangguan, Efficient photocatalytic hydrogen evolution on N-deficient $\text{g-C}_3\text{N}_4$ achieved by a molten salt post-treatment approach, *Appl. Catal. B: Environ.* 238 (2018) 465–470.

[63] W. Hu, W. Zhou, K. Zhang, X. Zhang, L. Wang, B. Jiang, G. Tian, D. Zhao, H. Fu, Facile strategy for controllable synthesis of stable mesoporous black TiO_2 hollow spheres with efficient solar-driven photocatalytic hydrogen evolution, *J. Mater. Chem. A Mater. Energy Sustain.* 4 (2016) 7495–7502.

[64] P. Ran, L. Jiang, X. Li, P. Zuo, B. Li, X. Li, X. Cheng, J. Zhang, Y. Lu, Redox shuttle enhances nonthermal femtosecond two-photon self-doping of $\text{rGO}/\text{TiO}_{2-x}$ photocatalysts under visible light, *J. Mater. Chem. A Mater. Energy Sustain.* 6 (2018) 16430–16438.

[65] Z. Fang, X. Huang, Y. Wang, W. Feng, Y. Zhang, S. Weng, X. Fu, P. Liu, Dual-defective strategy directing in situ assembly for effective interfacial contacts in MoS_2 cocatalyst/ In_2S_3 light harvester layered photocatalysts, *J. Mater. Chem. A Mater. Energy Sustain.* 4 (2016) 13980–13988.

[66] C. Yang, J. Qin, Z. Xue, M. Ma, X. Zhang, R. Liu, Rational design of carbon-doped TiO_2 modified $\text{g-C}_3\text{N}_4$ via in-situ heat treatment for drastically improved photocatalytic hydrogen with excellent photostability, *Nano Energy* 41 (2017) 1–9.

[67] S. Zhang, X. Liu, C. Liu, S. Luo, L. Wang, T. Cai, Y. Zeng, J. Yuan, W. Dong, Y. Pei, Y. Liu, MoS_2 quantum dot growth induced by S vacancies in a ZnIn_2S_4 monolayer: atomic-level heterostructure for photocatalytic hydrogen production, *ACS Nano* 12 (2018) 751–758.

[68] Y.-S. Xie, L. Yuan, N. Zhang, Y.-J. Xu, Light-tuned switching of charge transfer channel for simultaneously boosted photoactivity and stability, *Appl. Catal. B: Environ.* 238 (2018) 19–26.

[69] N. Meng, J. Ren, Y. Liu, Y. Huang, T. Petit, B. Zhang, Engineering oxygen-containing and amino groups into two-dimensional atomically-thin porous polymeric carbon nitrogen for enhanced photocatalytic hydrogen production, *Energy Environ.*

Sci. 11 (2018) 566–571.

[70] Z. Zhang, J. Huang, Y. Fang, M. Zhang, K. Liu, B. Dong, A nonmetal plasmonic Z-Scheme photocatalyst with UV- to NIR-driven photocatalytic protons reduction, *Adv. Mater.* 29 (2017) 1606688.

[71] N. Lu, Z. Zhang, Y. Wang, B. Liu, L. Guo, L. Wang, J. Huang, K. Liu, B. Dong, Direct evidence of IR-driven hot electron transfer in metal-free plasmonic $W_{18}O_{49}$ /carbon heterostructures for enhanced catalytic H_2 production, *Appl. Catal. B: Environ.* 233 (2018) 19–25.

[72] T.-T. Yang, W.-T. Chen, Y.-J. Hsu, K.-H. Wei, T.-Y. Lin, T.-W. Lin, Interfacial charge carrier dynamics in core-shell Au-CdS nanocrystals, *J. Phys. Chem. C* 114 (2010) 11414–11420.

[73] Y.-C. Chen, Y.-C. Pu, Y.-J. Hsu, Interfacial charge carrier dynamics of the three-component In_2O_3 - TiO_2 -Pt heterojunction system, *J. Phys. Chem. C* 116 (2012) 2967–2975.

[74] Z. Zhang, X. Jiang, B. Liu, L. Guo, N. Lu, L. Wang, J. Huang, K. Liu, B. Dong, IR-driven ultrafast transfer of plasmonic hot electrons in nonmetallic branched heterostructures for enhanced H_2 generation, *Adv. Mater.* 30 (2018) 1705221.

[75] J. Ran, T.Y. Ma, G. Gao, X.-W. Du, S.Z. Qiao, Porous P-doped graphitic carbon nitride nanosheets for synergistically enhanced visible-light photocatalytic H_2 production, *Energy Environ. Sci.* 8 (2015) 3708–3717.

[76] Z. Zhang, Y. Huang, K. Liu, L. Guo, Q. Yuan, B. Dong, Multichannel-improved charge-carrier dynamics in well-designed hetero-nanostructural plasmonic photocatalysts toward highly efficient solar-to-Fuels conversion, *Adv. Mater.* 27 (2015) 5906–5914.

[77] J. Wu, Z. Zhang, B. Liu, Y. Fang, L. Wang, B. Dong, UV-Vis-NIR-driven plasmonic photocatalysts with dual-resonance modes for synergistically enhancing H_2 generation, *Sol. Rrl* 2 (2018) 1800039.

[78] X. Wei, C. Shao, X. Li, N. Lu, K. Wang, Z. Zhang, Y. Liu, Facile in situ synthesis of plasmonic nanoparticles-decorated g - C_3N_4 / TiO_2 heterojunction nanofibers and comparison study of their photosynergistic effects for efficient photocatalytic H_2 evolution, *Nanoscale* 8 (2016) 11034–11043.

[79] H. Gao, H. Yang, J. Xu, S. Zhang, J. Li, Strongly coupled g - C_3N_4 Nanosheets- Co_3O_4 quantum dots as 2D/0D heterostructure composite for peroxymonosulfate activation, *Small* 14 (2018) 1801353.

[80] S. Zhang, H. Gao, Y. Huang, X. Wang, T. Hayat, J. Li, X. Xu, X. Wang, Ultrathin g - C_3N_4 nanosheets coupled with amorphous Cu-doped $FeOOH$ nanoclusters as 2D/0D heterogeneous catalysts for water remediation, *Environ. Sci. Nano* 5 (2018) 1179–1190.

[81] X. She, J. Wu, H. Xu, J. Zhong, Y. Wang, Y. Song, K. Nie, Y. Liu, Y. Yang, M.-T.F. Rodrigues, R. Vajtai, J. Lou, D. Du, H. Li, P.M. Ajayan, High efficiency photocatalytic water splitting using 2D α - Fe_2O_3 / g - C_3N_4 Z-Scheme catalysts, *Adv. Energy Mater.* 7 (2017) 1700025.